Wettability Variation and its Impact on CO_2 Storage Capacity at the Wyoming CarbonSAFE Storage Hub: An Experimental Approach

Ying Yu[1,*], Sumaiya Farzana[2], Charles Nye[1], Davin Bagdonas[1], Prashant R.Waghmare[2], Zunsheng Jiao[1], Jonathan Fred McLaughlin[1]

1. Center for Economic Geology Research, School of Energy Resources, University of Wyoming. 1000 E University Ave, Laramie, Wyoming, USA, 82071.
2. *Interfacial* Science & Surface Engineering Lab (*i*SSELab), Department of Mechanical Engineering, University of Alberta, Edmonton, Alberta T6G2G8, Canada

*Corresponding author, Email: yyu3@uwyo.edu

Abstract

Meeting global and national net zero carbon emission targets will require geologic carbon disposal. The U.S. Department of Energy (DOE) has accordingly funded significant research in this area, including the Wyoming CarbonSAFE project at Dry Fork Station (DFS) in Campbell County, Wyoming. This work studied wettability in micro- and macro-scales, CO_2 storage potential, and the correlation between the two to support the Wyoming CarbonSAFE project's subsurface assessment. During this study, a target formation's wettability was found to affect how much CO_2 can be stored in a given formation.

In this study, representative rock samples were selected from the target storage formations—Lakota, Hulett, and Minnelusa—based on the heterogeneity of the lithology, permeability, and porosity of the respective formations. The rock samples are all fine-grained sandstone with

variable cementation and bedding structure, including different scales of laminated bedding. The porosity and permeability vary within the range of 9.0–14.3% and 0.1–28.9 mD, respectively. These rock samples were prepared for the micro-scale wettability (contact angle measurement), macro-scale wettability (wettability index derived from unsteady-state flow characterization for the core plugs), and CO_2 storage potential and capacity evaluation. The macro-scale experiments suggested that wettability appeared to dominate the CO_2 storage potential performance during the drainage process, where less water-wet behavior promoted higher CO_2 storage potential. The micro-scale wettability tests showed that the rock samples at the studied reservoir conditions behaved water-wet and became more water-wet as pressure increased. This kind of wettability change discourages further CO_2 storage potential yet benefits the CO_2 residual trapping as the CO_2 injection proceeds for the studied area. The results allow the recommendation of the best storage candidate reservoir based on wettability that affects CO_2 storage. The work presented in this study provides valuable insights into wettability's effect on the CO_2 storage capacity and wettability's importance when identifying the optimal CO_2 storage formation to meet the project's goals.

1. Introduction

Global initiatives to reduce CO_2 emissions depend upon a smorgasbord of control techniques to meet all but the most modest goals. These multi-technology systems, especially in areas affected by the energy industry, almost always include CCUS [1,2]. This popularity results from CCUS's status as one of the most effective long-term techniques for isolating CO_2 from the atmospheric system. CCUS is also distinctive for enabling carbon-negative strategies such as direct air capture (DAC) or bioenergy with carbon capture and storage (BECCS), which have become increasingly important in the face of political inaction and delays [3]. In CCUS, CO_2 is pumped

into geologic formations such as depleted oil and gas reservoirs, deep saline aquifers, and coal bed formations, where CO_2 will react with local rocks and brines to form durable CO_2-bearing minerals that last for geologic time scales. Varying by the storage site, different trapping mechanisms prevent the CO_2 from leaking to the surface: (1) structural trapping, (2) capillary or residual trapping, (3) dissolution trapping, and (4) mineral trapping.

The viability of some of these trapping mechanisms depends upon the wettability of the storage system [3]. Wettability affects CO_2 structural trapping and capillary trapping in slightly different ways. For structural trapping, where the caprock serves as the sealing formation that retains CO_2 in place, one concern is that the wettability of the caprock may alter during the CO_2 sequestration process. A 38% difference in contact angle could manifest in a 5–10% difference in capillary pressure [4]. As a result, a CO_2 capillary leak might happen when injection pressure surpasses the current capillary pressure of the caprock, which substantially limits the CO_2 storage capacity. Capillary/residual trapping increases storage security over structural trapping by reducing the severity of capillary leaks and has been a significant research area since being considered in the IPCC's 2005 report [4]. Capillary/residual trapping occurs when CO_2 is immobilized in the pore space and surrounded by brine due to imbibition after initial displacement. The effectiveness of this immobilization depends on the fluid physics, phase behavior, and the pore size of the rock [5]. When CO_2 moves into a rock, the piston-like advance suppresses trapping, while the wetting layer and snap-off mechanism lead to enhanced trapping as the wetting phase fills the pore-throats and strands the non-wetting phase in pores, where the high flow rate favors piston-like advance instead of trapping. A change in wettability will not only affect the cap rock sealing capacity but also affect the residual trapping, where a less water-wet rock results in less CO_2 residual trapping. Krever et al.[5] stated that the success of residual trapping is dominated by

wettability, pore-throat size ratio, and connectivity, whereas residual trapping is enhanced by a highly water-wet rock, large pore-throat size ratio, and poor connectivity. A highly water-wet rock surface for the long-term imbibition process is preferred. Yet, the displacement of reservoir fluids during the CO_2 drainage process sets the baseline of pore space utilization for the subsequently injected CO_2 to be stored—CO_2 storage potential [6]. Thus, an established understanding of the wettability effect on the CO_2 storage potential is needed for any CCUS storage assessment.

Wettability is normally determined by the contact angle method, Amott method, USBM method, and combined Amott and USBM method [7–11]. The contact angle method is often adopted due to the relatively low cost, where it is the best wettability method for pure fluid and a pure crystal idealization of rock. The sessile drop method and captive bubble method for contact angle measurement are generally used in the oil and gas industry, where a droplet is placed by a syringe on a single flat polished mineral surface or a small piece of the reservoir rock. The droplet profile of the fluid is captured by a high-resolution camera and analyzed by the software to deliver the contact angle values over time. The type of angles to be measured is also important: static angles or advancing and receding angles; when reaching equilibrium, one equilibrium static contact angle is determined. When gradually increasing or decreasing the droplet volume, the advancing and receding angle can be obtained. Farzana et al. found that increased pressure reduces droplet spreading radius and increases advancing contact angle during the spreading of the droplet with constant mass flux, through both theoretical and experimental observations [12,13]. Sarmadivaleh et al. suggested that larger water advancing contact angle implies less structural and residual trapping for CO_2 at high pressure and temperature [7]. Both static and advancing/receding angles have been studied [7–9], where the temperature, pressure, brine

92 composition, salinity, and the composition and roughness of the substrate all play significant
93 roles in the actual value of the contact angle, which serves as an indication of wettability. The
94 contact angle method measures a small piece of reservoir rock's wettability, representing the
95 wettability at the micro-scale. This means it may not be illustrative at the reservoir scale. The
96 compositional heterogeneity and complex geometry of reservoir rocks could also cause
97 wettability variation at the pore scale. Thus, it is essential to carefully select samples to ensure
98 the samples are representative of the target reservoirs' wettability. Amott and USBM methods,
99 on the other side, measure the wettability of a core sample. The Amott method uses four
100 spontaneous/forcibly displacement processes of brine and oil [14]. Donaldson et al. [11]
101 established a method to determine the wettability index, the USBM wettability index, from the
102 hysteresis loop of capillary pressure curves. The capillary pressure curves are obtained by
103 alternately displacing water and oil from small core plugs using a centrifuge. The areas under the
104 capillary pressure curves show the thermodynamic effort required for the respective fluid
105 displacement. Thus, the wettability could be determined by comparing the areas as water-wet,
106 oil-wet, or neutral-wet. In addition to the above method, recently, Mirzaei-Paiaman presented a
107 work of determining the wettability from the relative permeability based on Craig's three rules of
108 thumb [15,16], where the Lax Index I_{kr} is introduced. For a strongly water-wet sample I_{kr}
109 advances toward $+1$, while for a strongly oil-wet sample I_{kr} tends to -1. This study adopted the
110 Lax Index that extrapolated from the relative permeability curves, interpreted from the CO_2
111 drainage process as the wettability indicator at the macro-scale.

112 The Wyoming CarbonSAFE project at DFS in Campbell County, Wyoming, is one of the
113 flagship CCUS projects in the United States. The project conducts the site characterization and
114 assessment to determine how 50 MT of CO_2 could be permanently stored at the site during 30

115 years of operations. CO_2-water fluid flow system characterization is critical to modeling this
116 storage capacity and showing safe containment of CO_2 within the commercial-scale CCUS
117 project. In this study, rock samples were selected from the target storage formations (the Lower
118 Cretaceous Lakota Sandstone, Jurassic Hulett Sandstone, and Pennsylvanian Minnelusa B, C,
119 and D formations near DFS) based on how well they would represent the lithology, permeability,
120 and porosity of the respective formations. The rock samples are all fine-grained sandstones with
121 sedimentation, cementation, and lamination variance. The porosity and permeability vary
122 between 9.0–14.3% and 0.1–28.9 mD, respectively. These rock samples were prepared for the
123 micro-scale wettability (contact angle measurement), macro-scale wettability (wettability index
124 derived from unsteady-state flow characterization for the core plugs), and CO_2 storage potential
125 and capacity evaluation. The macro-scale experiments suggested that wettability appeared to
126 dominate the CO_2 storage potential performance during the drainage process, where less water-
127 wet behavior promoted higher CO_2 storage potential. The micro-scale wettability tests showed
128 that the rock samples at the studied reservoir conditions behaved water-wet and became more
129 water-wet as pressure increased. This kind of wettability change discourages further CO_2 storage
130 potential yet benefits the CO_2 residual trapping as the CO_2 injection proceeds for the studied area.
131 The CO_2 storage evaluation presented in this study allows wettability effects to be propagated
132 into geologic consideration of the site and adds nuance to the ranking of the reservoirs. Armed
133 with this knowledge, CarbonSAFE project leads will be more confident in meeting their CCUS
134 project's goals.

135 ## 2. Materials and Methods

136 ### 2.1. Rock Samples and synthetic formation water

The rock samples used for the micro- and macro-scale wettability tests are listed in this section. Note that there is some inconsistency between the two selections of rock samples due to unavailability. However, similar samples nearby were used as the substitution.

2.1.1 Rock samples for micro-scale wettability determination

Contact angle (CA) measurements were conducted for the selected rock samples from each formation targeted for CCUS storage at the DFS site as the micro-scale wettability determination method. The interfacial tension (IFT) tests were performed along with the contact angle measurements. The representative rock samples of each formation were carefully selected based on the thin-section results, combinable magnetic resonance, gamma-ray, mud logs, and average permeabilities and porosities. In addition, the formation pressure and temperature were extrapolated from the Modular Dynamic Tester (MDT) log. In addition to the nine samples of reservoir rock, two sealing formation samples (Fuson and Opeche shales) were also tested. **Table 1** tabulates the experimental temperature and pressure of the rock samples for interfacial tension (IFT) and contact angle (CA) tests, respectively.

Table 1 Experimental information for IFT and CA measurement tests

MD (ft)	Sample No.	Formation	Lithology	Temperature (F)	Formation Pressure (psi)	Pressure #2 (psi)	Pressure #3 (psi)
7970.0	1	Fuson	Shale	178	2839	3985	4384
8035.4	2	Lakota	Sandstone	179	2929	4018	4419
8039.4	3	Lakota	Sandstone	179	2934	4020	4422
8307.7	4	Hulett	Sandstone	182	3303	4154	4569
8332.6	5	Hulett	Sandstone	183	3337	4166	4583
9329.3	6	Opeche	Shale	176	3776	4665	5131
9367.6	7	Minnelusa B	Sandstone	181	3815	4684	5152
9392.0	8	Minnelusa B	Sandstone	184	3840	4696	5166
9480.6	10	Minnelusa C	Sandstone	195	3961	4740	5214
9529.3	11	Minnelusa D	Sandstone	202	4007	4765	5241

153 The selected rock samples were cut into 15 × 10 × ~5 mm squares and polished with 320 grit
154 sandpaper, 800 grit sandpaper, and then Hyperion water-soluble diamond polishing pastes (12, 8,
155 4, and 2 microns). After polishing, the rock samples were cleaned in a soxhlet extractor with 1:1
156 methanol and toluene at 110 ℃ for 72 hrs and dried in an oven at 110 ℃ for another 72 hrs to
157 remove any trace of contaminates [17]. Then, the surface roughness of the rock samples was
158 assessed using LEXT OLS4000 3D Laser Scanning Microscope. The surface roughness
159 information is included in **Supporting Material**. **Fig. 1** displays the selected rock samples after
160 cutting, polishing, and cleaning.

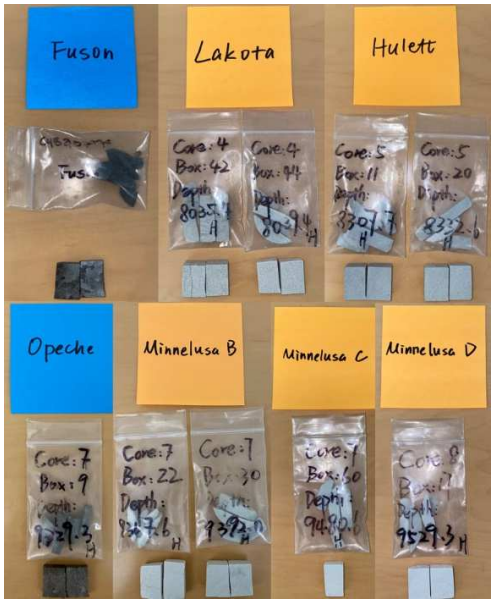

161

162 **Fig. 1.** The selected rock sample after cutting, polishing, and cleaning.

163 The correlation between the measured depth and formation pressure in **Table 1** illustrates that
164 the target area in Powder River Basin is under-pressured as the calculated hydrostatic pressure
165 gradient ranges from 0.356 to 0.421 psi/ft. It has been reported that the normal hydrostatic
166 pressure gradient is 0.433 psi/ft in the freshwater reservoirs and 0.5 psi/ft in very saline
167 reservoirs in the Rocky Mountain region [18,19]. Spencer *et al.* considered reservoirs to be
168 significantly over-pressured if the pressure gradient exceeds 0.50 psi/ft in basins with fresh to

moderately saline water and 0.55 psi/ft in basins with very saline water. Therefore, to get a more robust profile of the wettability changes, where the reservoir pressure will naturally increase due to CO_2 injection, the second and third sets of pressures calculated with 0.5 psi/ft and 0.55 psi/ft were also chosen for the IFT tests, while the third set of pressures calculated with 0.55 psi/ft was conducted for contact angle measurements (**Table 1**).

2.1.2 Rock samples for macro-scale wettability determination and CO_2 storage evaluation

Nine core plugs from the Lakota, Hulett, and Minnelusa formations at the DFS storage were selected based on thin-section observations, combinable magnetic resonance, gamma-ray, mud logs, and average permeabilities and porosities for target formations. The formation pressure and temperature were extrapolated from the Modular Dynamic Tester (MDT). Gas porosity and permeability measurements were carried out under a net confining pressure of 1000 psi, either with a Coreval 700 permeameter and porosimeter (VINCI Technologies, France) or sent to Core Laboratories Petro Services (Denver, CO). In this work, the overburden/confining pressures were not set to their full values, where the overburden gradient is referred to 1.0-1.1 psi/ft [20]. However, based on another study [21], where the authors discussed the response of the porosity and permeability to the effective stress, the porosity and permeability of Darley Dale (the closest sample in literature with porosity and permeability near to the samples used in this study) changed from 13.5% and 21.6 mD to 12.7% and 7.0 mD from 1450 psi to 5802 psi, which are considered not drastic with respect to the scope of this work. Thus, the overburden/confining pressures were kept as lower values (net confining pressure 1000 psi). **Table 2** tabulates the experimental information and petrophysical properties of the core plugs. Here, Klinkenberg-corrected gas permeabilities (considering the Klinkenberg gas slippage effect) are reported for the nine reservoir samples.

192 **Table 2** The experimental information and petrophysical properties of the core plugs.

MD (ft)	Sample No.	Formation	Lithology	Temperature (°F)	Formation Pressure (psi)	Porosity (%)	Corrected gas Permeability (mD)	Water Permeability (mD)
8031.4	1	Lakota	Sandstone	178	2923	13.479	28.926	20.802
8035.4	2	Lakota	Sandstone	179	2929	13.873	14.160	13.105
8307.7	3	Hulett	Sandstone	182	3303	9.137	0.124	0.006
8325.8	4	Hulett	Sandstone	183	3328	13.074	3.463	2.206
8332.6	5	Hulett	Sandstone	183	3337	14.305	8.056	5.346
9366.8	6	Minnelusa B	Sandstone	181	3814	12.756	11.146	8.700
9457.8	7	Minnelusa C	Sandstone	193	3939	11.169	38.914	34.382
9464.2	8	Minnelusa C	Sandstone	193	3945	9.014	2.512	1.987
9529.3	9	Minnelusa D	Sandstone	202	4007	10.096	18.338	18.780

193

194 ### 2.1.3. Synthetic formation water

195 The small-volume formation water samples were collected during MDT and analyzed by ICP-
196 OES (cations) and Ion Chromatography (anions). From this analysis, we designed a synthetic
197 formation water (SFW) to provide adequate water volumes for testing each target storage
198 formation listed in **Table 3**. Due to the moderate mixing of formation water with drilling fluids
199 while sampling with the MDT, the salinity of these waters is higher than in-situ, and they
200 therefore present a pessimistic case for geochemical reactions – although no reaction was
201 observed.

202 **Table 3** Synthetic formation water formulation

Component	Conc. (mg/L)				
	Lakota	Hulett	Minnelusa B	Minnelusa C	Minnelusa D
KCl	6,349.42	9,514.60	7,550.66	3,470.25	7,779.47
NaCl	45,401.96	82,000.44	81,862.43	47,299.70	80,757.80
$CaCl_2 \cdot 2H_2O$	3,216.77	4,658.26	4,181.43	2,776.62	4,181.43

$MgCl_2 \cdot 6H_2O$	33.46	58.55	485.16	769.57	267.68
Na_2SO_4	4,859.87	7,630.58	7,497.23	6,474.88	8,512.18
Na_2CO_3	0.14	0.14	0.16	0.14	0.16
$NaHCO_3$	1,135.75	1,090.32	1,266.53	1,115.10	1,300.95

2.2. Experimental setup and procedures

2.2.1 Micro-scale wettability determination: CA and IFT measurements

A high pressure and high temperature (HPHT) interfacial tension (IFT) and contact angle (CA) measurement system (**Fig. 2**, DSA 100 HPHT, Krüss, Hamburg) was deployed for IFT tests between SFW and CO_2 and CA tests of CO_2 droplets on formation rock samples in SFW.

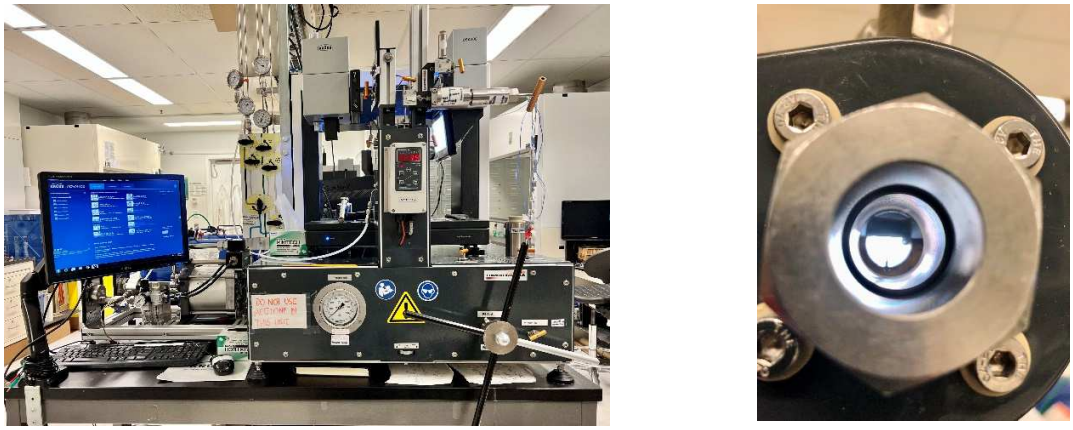

(a) (b)

Fig. 2 (a) DSA 100 HPHT unit (KRÜSS GmbH – Germany), (b) measuring chamber

The SFW formulation for each formation was prepared using the information given in **Table 3.** The rock samples were soaked in SFW for 72 hours at the reservoir temperature before taking the measurements. After the attempt to restore the native wettability, the rock sample was transferred to the measuring chamber of the DSA 100 HPHT system (**Fig. 2b**). Then, the measuring chamber was closed and filled with SFW to completely submerge the substrate. To saturate the SFW, the chamber temperature was increased to meet the desired reservoir temperature, and CO_2 was injected into the system to meet the reservoir pressure. After one hour,

a gas pressure reduction inside the chamber was observed, which indicates the dissolution of CO_2 in the solution. Extra CO_2 was then injected into the cell to saturate the SFW at the target measuring pressure. The system was then left idle to achieve equilibration for eight hours at the selected reservoir pressure and temperature before taking measurements. The pendant drop method is adopted for the IFT test against CO_2. The test is conducted for a CO_2 droplet when it is attached to the capillary tube, pre-releasing to the rock surface. To generate a CO_2 bubble for IFT measurement, some amount of gas was allowed to pass through the needle at a very low flow rate to make a bubble, as shown in **Fig. 3**.

(a) (b)

Fig. 3 (a) CO_2 bubble formation for IFT measurement; (b) CO_2 bubble on the substrate for CA measurement.

To measure the equilibrium CA, the CO_2 bubble was released from the tube so that it subsequently spread under the rock substrate. Upon reaching a static state, equilibrium CA was measured. DSA 100 camera was used to capture the images at the frame rate of 50 fps. Images were then analyzed using ADVANCE software for IFT and CA determination. The equilibrium densities of both CO_2 and SFW were calculated for each reservoir condition using Geochemists' Workbench 11 and considering SFW in the presence of CO_2. No precipitation was found during the calculation. The densities used for IFT and CA calculations are tabulated in **Table 4**.

231 **Table 4** CO_2 and SFW densities for each sample at the respective reservoir conditions

Fluid			CO_2	Synthetic Formation Water				
				Lakota	Hulett	Minn B	Minn C	Minn D
1st set of densities for formation pressure								
MD (ft)	**Pressure (psi)**	**Temperature (°F)**	**Density (g/cm3)**					
7970.0	2839	178	0.57879	1.07629				
8035.4	2929	179	0.58848	1.07669				
8039.4	2934	179	0.58913	1.07672				
8307.7	3303	182	0.63242		1.10646			
8332.6	3337	183	0.63344		1.1065			
9329.3	3776	176	0.69947			1.10946		
9367.6	3815	181	0.68962			1.10859		
9392.0	3840	184	0.68398			1.10814		
9476.8	3957	195	0.66660				1.07817	
9480.6	3961	195	0.66698				1.07819	
9529.3	4007	202	0.65393					1.10716
2nd set of densities for pressure #2 calculated with 0.5 psi/ft								
MD (ft)	**Pressure (psi)**	**Temperature (°F)**	**Density (g/cm3)**					
7970.0	3985	178	0.71257	1.08467				
8035.4	4018	179	0.71278	1.08465				
8039.4	4020	179	0.71295	1.08467				
8307.7	4154	182	0.71642		1.1128			
8332.6	4166	183	0.71492		1.11268			
9329.3	4665	176	0.76634			1.11604		
9367.6	4684	181	0.75647			1.11505		
9392.0	4696	184	0.75062			1.11453		
9476.8	4738	195	0.72931				1.08399	
9480.6	4740	195	0.72944				1.084	
9529.3	4765	202	0.71602					1.11297
3rd set of densities for pressure #3 calculated with 0.55 psi/ft								
MD (ft)	**Pressure (psi)**	**Temperature (°F)**	**Density (g/cm3)**					
7970.0	4384	178	0.74331	1.09022				
8035.4	4419	179	0.74343	1.09006				
8039.4	4422	179	0.74364	1.09007				
8307.7	4569	182	0.74678		1.11778			
8332.6	4583	183	0.74546		1.11763			
9329.3	5131	176	0.79246			1.1189		
9367.6	5152	181	0.78335			1.11786		
9392.0	5166	184	0.77799			1.11729		

9476.8	5212	195	0.75827	1.08656	
9480.6	5214	195	0.75838	1.08656	
9529.3	5241	202	0.74591		1.11537

232

233 **2.2.2 CO_2 storage evaluation and macro-scale wettability determination**

234 The above-discussed nine lithological and petrophysical representative core plugs from five
235 target storage formations (Lakota, Hulett, Minnelusa B, Minnelusa C, and Minnelusa D) at the
236 DFS storage site were chosen for CO_2 storage evaluation and macro-scale wettability
237 characterization through drainage and imbibition processes utilizing the project-oriented core
238 flooding system, as illustrated in **Fig. 4**.

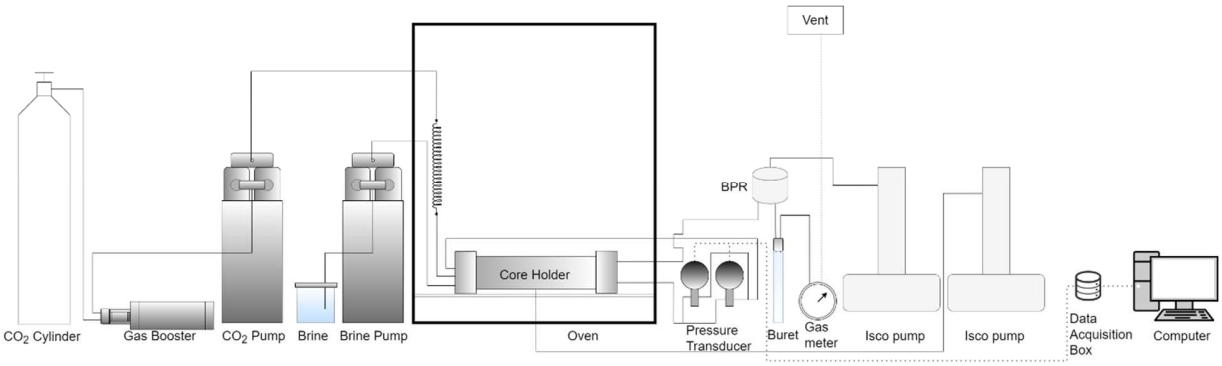

239

240 **Fig. 4** Schematic diagram of core flooding system

241 The core flooding system was integrated with two dual-cylinder Vindum pumps for controlling
242 SFW and CO_2 injection. A Haskel gas booster compressed the CO_2 to the target reservoir
243 pressures. Two Teledyne ISCO pumps (260D) were utilized to provide the net confining pressure
244 of 1000 psi throughout all experiments and maintain the pressure of the back pressure regulator
245 (CoreLabs, 5,000 psi capacity). In addition, two Rosemount™ pressure transducers with
246 different measuring ranges, 0–300 psi and 0–2,000 psi, were used to monitor the pressure drop
247 across the core plug. Finally, the core holder was placed inside the Memmert UF750 oven to
248 achieve the desired temperature.

249 Similar to the rock sample preparation for contact angle test, the core plugs were initially cleaned
250 and dried. After the cleaning and drying steps, core plugs were wrapped with Teflon tape,
251 aluminum foil, and a shrink tube. The wrapped core plugs were vacuumed and saturated with
252 SFW for 12 hours. Then, the core plugs were immersed in the SFW in a sealed container at the
253 reservoir temperature for 30 days to restore wettability. The core plugs were vacuum-saturated
254 again to ensure complete saturation before loading into the Hastelloy core holder and installed
255 horizontally inside the oven. To determine water permeability, a continuous SFW injection was
256 performed at different flow rates (0.05 – 0.5 mL/min). The water permeability of all tested core
257 plugs is also listed in **Table 2**. All experiments were conducted at the respective temperature and
258 pressure listed in **Table 2** with a net confining pressure of 1,000 psi.

259 After the water permeability measurement, CO_2 was injected at flow rates of 0.2 – 0.5 g/min
260 (volume rate slightly varies depending on samples' reservoir conditions) to displace the water
261 until irreducible water saturation was met when no more water was produced during an average
262 of 1.56 PV addition CO_2 injection. The original water in place that CO_2 has displaced indicated
263 the CO_2 storage potential. Therefore, the approximation of CO_2 storage potential and CO_2

storage capacity in the corresponding core sample was calculated with the formula shown in Eq. 1 and Eq. 2, respectively:

$$CO_2\ storage\ potential\ (\%) = \frac{Volume\ of\ water\ displaced}{Rock's\ pore\ volume} \times 100\% \quad \text{(Eq. 1)}$$

$$CO_2\ storage\ capacity\ (\%) = CO_2\ storage\ potential\ (\%) * Porosity\ (\%) \quad \text{(Eq. 2)}$$

where the CO_2 storage potential focuses on the pore space utilization, and the CO_2 storage capacity considers the formation as a bulk.

The steady-state relative permeability method is where multiphase fluids are co-injected, and relative permeability data are recorded when the conditions in the core are stabilized [22]. The steady-state method is usually more accurate, especially for the natural heterogeneous porous media; however, it is more time-consuming than the unsteady-state method, where dynamic displacement is performed [23,24]. The dynamic displacement method and calculation were depicted in detail in Johnson et al.'s work [23]. This is the so-called Johnson-Bossler-Naumann (JBN) solution, the industry standard for unsteady-state measurement. The relative permeability interpretation in this work was conducted utilizing the unsteady-state method and mass balance saturation determination. In addition, higher flow rates help minimize the capillary end effect [22,25]; therefore, higher yet typical flow rates are preferred. Thus, at least two injection rates were adopted for each sample.

Following the drainage process, SFW was injected at the flow rate of either 0.2 or 0.05 mL/min; this is considered an imbibition process. Once the pressure drop across the core became relatively constant and water saturation stopped increasing, the test for one core plug ended. The mass-balance calculations were conducted to estimate the water saturation. Water production during both CO_2 and SFW injection was measured volumetrically using a gas-tight 25 mL buret.

A Ritter gas meter TG 0.5/5 was connected to the buret with an air-tight seal to record the produced CO_2 flow rate and volume. The dead volume was minimized by using the smaller inner diameter (0.030 inch) 1/8 inch tubing and measured before testing to allow for better injection monitoring. The pressure drop during gas/SFW injection as a function of time was recorded. At the end of each drainage/imbibition test, CO_2 storage potential was checked to evaluate the CO_2 storage capacity/residual trapping for each sample.

All flow rates mentioned above are at reservoir conditions. The CO_2 density and viscosity at each core plug's respective reservoir conditions were extrapolated from the National Institute of Standards and Technology (NIST) Standard Reference Database and Ouyang's improved CO_2 density and viscosity calculation, which has good agreement with NIST data [26,27]. The relative permeability interpretation has considered the CO_2 and brine solubility and assumed fully-saturated brine and injected CO_2 by adopting Duan *et al.* [28,29]. The density and viscosity of CO_2 are tabulated in **Table 5**.

Table 5 CO_2 density and viscosity at each core plug's respective reservoir conditions

MD (ft)	Formation	Pressure (psi)	Temperature (°F)	density (g/cm3)	viscosity (cP)
8031.4	Lakota	2923	178	0.5895	0.0457
8035.4	Lakota	2929	179	0.5900	0.0457
8307.7	Hulett	3303	182	0.6309	0.0499
8325.8	Hulett	3328	183	0.6331	0.0502
8332.6	Hulett	3337	183	0.6339	0.0503
9366.8	Minnelusa B	3814	181	0.6894	0.0566
9457.8	Minnelusa C	3939	193	0.6712	0.0547
9464.2	Minnelusa C	3945	193	0.6697	0.0545
9529.3	Minnelusa D	4007	202	0.6550	0.0530

300 ## 3. Results and Discussion

301 ### 3.1. Micro-scale wettability determination

302 Micro-scale wettability (CA) tests along with the IFT tests, were conducted with the SFW and
303 rock samples introduced in **Sections 2.1.3 and 2.1.1**. The following subsections describe the
304 interfacial tension, contact angle, and wettability effect on CO_2 storage. The capillary pressure
305 interpretation for sealing formation Fuson and Opeche is also included.

306 #### 3.1.1. IFT between the SFW and CO_2 for target formations at the reservoir conditions

307 When CO_2 is introduced into reservoir formations, the reservoir brine interacts with CO_2 and
308 generates various compounds, i.e., dissolved CO_2, carbonate, bicarbonate, and hydrogen ions,
309 depending on pH, and lowers pH down to 3 [30]. Thus, the water molecules on the rock surface
310 had decreased surface tension. This study reports the surface tension of five different salinity
311 brines against CO_2 (**Table 6**). After the completion of the equilibration process for eight hours,
312 the IFT was measured by forming a CO_2 bubble at the tip of the needle, as shown in **Fig. 3a**. The
313 time-averaged IFT value is recorded prior to the detachment of the drop from the needle. It takes
314 approximately 8 to 10 mins for the drop to detach from the needle depending on the surrounding
315 SFW, pressure and temperature.

316 **Table 6** Interfacial tension between the SFW and CO_2

Pressure set #1 - reservoir pressure					
MD (ft)	**Formation**	**Temperature (°F)**	**Formation Pressure (psi)**	**Mean IFT (mN/m)**	**1.96 SE**
7970.0	Fuson	178	2839	35.77	0.66
8035.4	Lakota	179	2929	35.53	0.40
8039.4	Lakota	179	2934	34.43	0.39
8307.7	Hulett	182	3303	35.77	0.27
8332.6	Hulett	183	3337	34.71	0.10
9329.3	Opeche	176	3776	35.40	0.05
9367.6	Minnelusa B	181	3815	35.51	0.03
9392.0	Minnelusa B	184	3840	35.75	0.30

9480.6	Minnelusa C	195	3961	31.06	0.10
9529.3	Minnelusa D	202	4007	35.71	0.47

Pressure set #2

MD (ft)	Formation	Temperature (°F)	Formation Pressure (psi)	Mean IFT (mN/m)	1.96 SE
7970.0	Fuson	178	3985	35.85	0.03
8035.4	Lakota	179	4018	36.60	1.25
8039.4	Lakota	179	4020	36.72	0.74
8307.7	Hulett	182	4154	35.99	0.23
8332.6	Hulett	183	4166	34.72	0.16
9329.3	Opeche	176	4665	35.57	0.44
9367.6	Minnelusa B	181	4684	35.69	0.65
9392.0	Minnelusa B	184	4696	36.67	0.14
9480.6	Minnelusa C	195	4740	31.34	0.03
9529.3	Minnelusa D	202	4765	35.90	0.21

Pressure set #3

MD (ft)	Formation	Temperature (°F)	Formation Pressure (psi)	Mean IFT (mN/m)	1.96 SE
7970.0	Fuson	178	4384	36.43	1.94
8035.4	Lakota	179	4419	36.92	0.53
8039.4	Lakota	179	4422	36.74	0.44
8307.7	Hulett	182	4569	36.08	0.23
8332.6	Hulett	183	4583	38.15	0.37
9329.3	Opeche	176	5131	36.68	0.42
9367.6	Minnelusa B	181	5152	36.84	0.50
9392.0	Minnelusa B	184	5166	36.97	0.43
9480.6	Minnelusa C	195	5214	31.44	0.10
9529.3	Minnelusa D	202	5241	36.83	0.24

Three readings were recorded for each sample, and the mean values are listed in **Table 6**. In all cases, the average IFT increased with increasing pressure for each sample, as shown in **Fig. 5**. As pressure increases, the intermolecular force of attraction inside the CO_2 bubble increases. As a result, the IFT increases with pressure at a specific temperature.

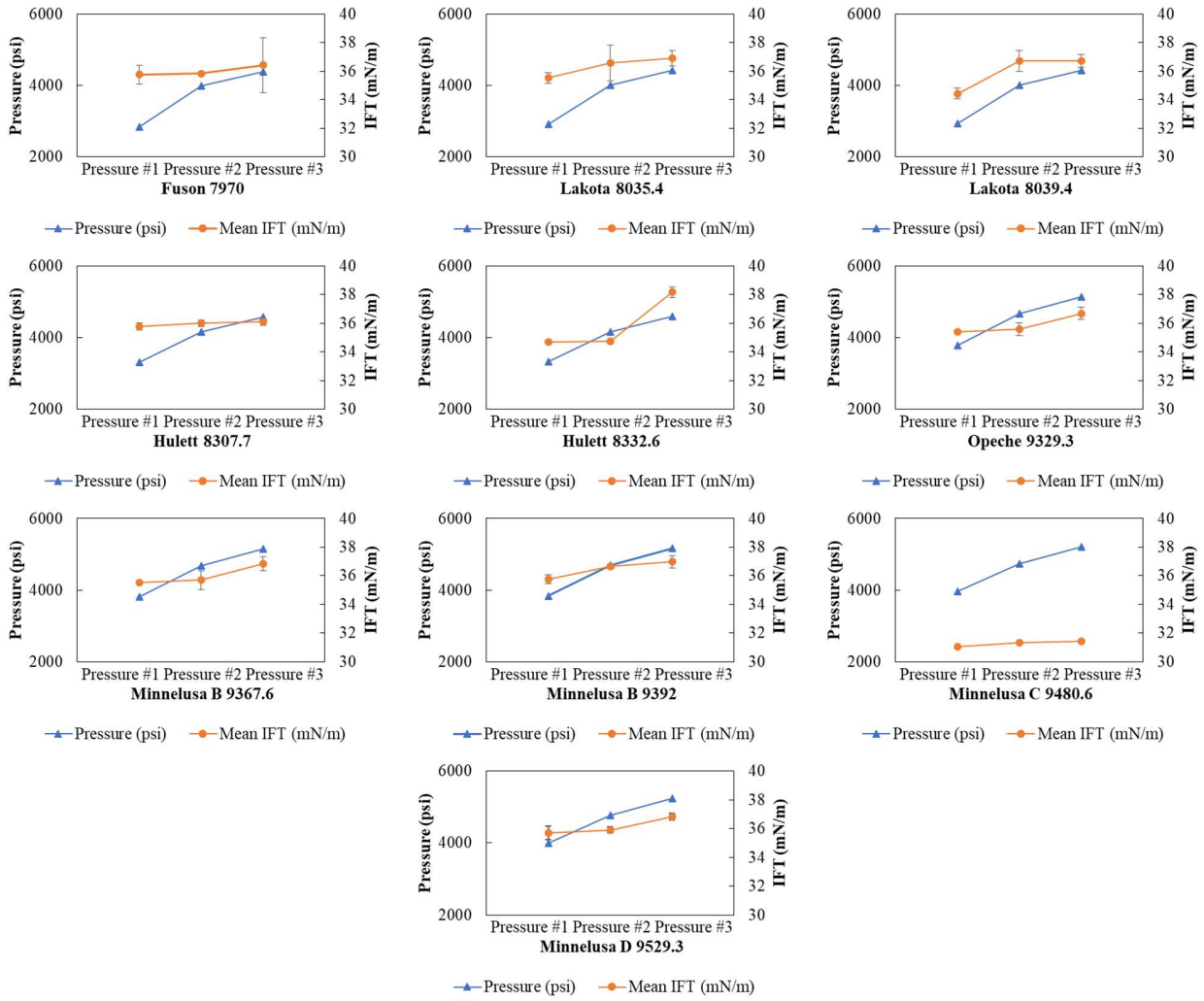

Fig. 5 Interfacial tension between brine and CO_2 at elevated temperatures and three pressures

3.1.2. CO_2-SFW-Rock system CA for target formations at the reservoir conditions

After the eight-hour CO_2-SFW-Rock equilibration, a fresh CO_2 droplet was released onto the rock surface. Once the CO_2 droplet completely spread, the CA was recorded for the next 30 mins. In the tests of Fuson 7970, Lakota 8035.4, Hulett 8307.7, Hulett 8332.6, and Minnelusa D 9529.3, the droplets did not stay on the substrate long enough because of their super-hydrophobic behavior. CA for these substrates was measured at the first instance the bubble made contact with the substrate after deposition. For Lakota 8039.4, Opeche 9329.3, Minnelusa B 9367.6,

330 Minnelusa B 9392, and Minnelusa C 9480.6, the droplets stayed at the surface for the entire 30

331 mins, which is depicted in **Fig. 6a**.

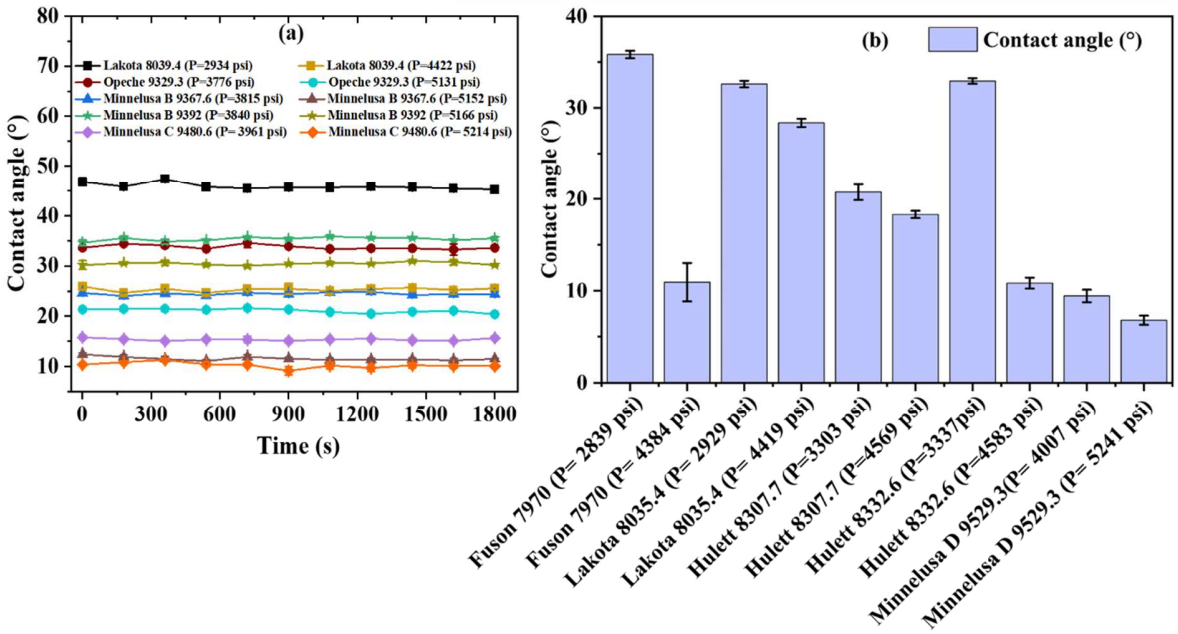

332

333 **Fig. 6** (a) Change of contact angle with time for Lakota 8039.4, Opeche 9329.3, Minnelusa B
334 9367.6, Minnelusa B 9392.0, and Minnelusa C 9480.6 substrates at the pressure set #1 and #3 (b)
335 Contact angle value at pressure set #1 and #3 for the substrates where the CO_2 bubble does not
336 stay long enough after deposition.

337 **Table 7** CA results at three sets of pressure

Pressure set #1 - reservoir pressure						
MD (ft)	**Formation**	**Temperature (°F)**	**Formation Pressure (psi)**	**CA (°)**	**1.96 SE**	**Wettability** [31]
7970.0	Fuson	178	2839	35.83	0.46	Moderately water-wet
8035.4	Lakota	179	2929	32.60	1.11	Moderately water-wet
8039.4	Lakota	179	2934	45.80	0.41	Moderately water-wet
8307.7	Hulett	182	3303	20.73	0.97	Strongly water-wet
8332.6	Hulett	183	3337	32.93	0.35	Moderately water-wet
9329.3	Opeche	176	3776	34.60	1.11	Moderately water-wet
9367.6	Minnelusa B	181	3815	24.40	0.45	Strongly water-wet
9392.0	Minnelusa B	184	3840	35.80	0.23	Moderately water-wet
9480.6	Minnelusa C	195	3961	15.37	0.74	Strongly water-wet
9529.3	Minnelusa D	202	4007	9.43	0.77	Strongly water-wet
Pressure set #2						
MD (ft)	**Formation**	**Temperature**	**Formation Pressure**	**CA (°)**	**1.96 SE**	

		(°F)	(psi)			
7970	Fuson	178	3985	18.87	0.47	Strongly water-wet
8035.4	Lakota	179	4018	30.20	1.08	Moderately water-wet
8039.4	Lakota	179	4020	29.07	0.85	Strongly water-wet
8307.7	Hulett	182	4154	19.57	1.43	Strongly water-wet
8332.6	Hulett	183	4166	20.80	0.45	Strongly water-wet
9329.3	Opeche	176	4665	23.73	0.53	Strongly water-wet
9367.6	Minnelusa B	181	4684	14.33	0.57	Strongly water-wet
9392	Minnelusa B	184	4696	31.93	0.80	Moderately water-wet
9480.6	Minnelusa C	195	4740	14.23	0.36	Strongly water-wet
9529.3	Minnelusa D	202	4765	9.40	1.08	Strongly water-wet
			Pressure set #3			
MD (ft)	**Formation**	**Temperature (°F)**	**Formation Pressure (psi)**	**CA (°)**	**1.96 SE**	
7970	Fuson	178	4384	10.93	2.36	Strongly water-wet
8035.4	Lakota	179	4419	28.37	0.51	Strongly water-wet
8039.4	Lakota	179	4422	25.47	1.27	Strongly water-wet
8307.7	Hulett	182	4569	18.30	0.45	Strongly water-wet
8332.6	Hulett	183	4583	10.83	0.66	Strongly water-wet
9329.3	Opeche	176	5131	21.67	0.79	Strongly water-wet
9367.6	Minnelusa B	181	5152	11.57	0.28	Strongly water-wet
9392	Minnelusa B	184	5166	30.43	0.24	Moderately water-wet
9480.6	Minnelusa C	195	5214	9.17	0.94	Strongly water-wet
9529.3	Minnelusa D	202	5241	6.80	0.57	Strongly water-wet

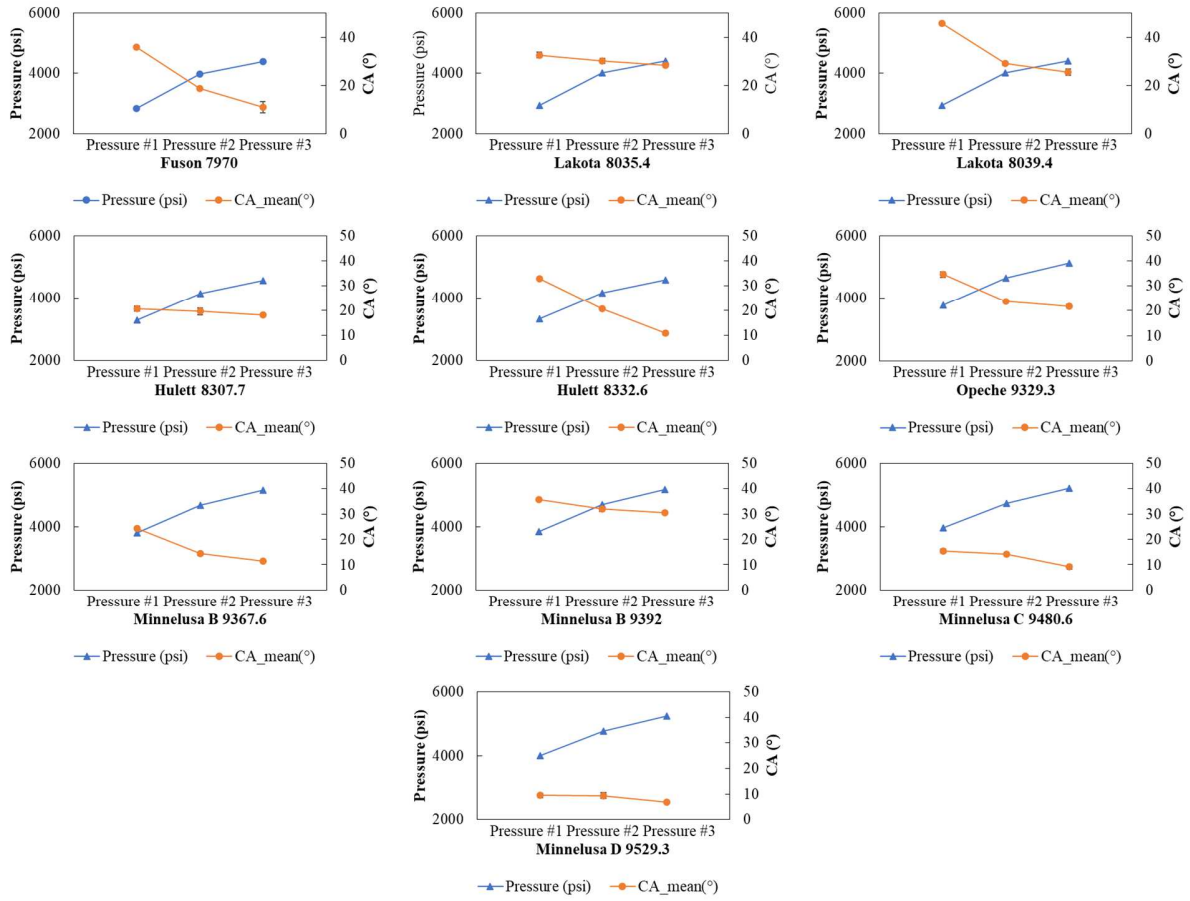

338

339 **Fig. 7** CO_2-SFW-Rock CA at elevated temperatures and three pressures.

340 **Table 7** and **Fig. 7** display the CA results for all samples at pressure sets #1, #2, and #3. All the
341 samples behaved strongly (CA = 0–30°) to moderately (CA = 30–75°) water-wet [31] at the
342 reservoir pressure and became strongly water-wet as the pressure increased. The wettability
343 alteration at the rock surface was rather significant for all samples with respect to contact angle,
344 especially for Fuson 7970.0, Lakota 8039.4, Hulett 8332.6, Opeche 9329.3, and Minnelusa B
345 9367.6, where the CA changed more than 10°. The CO_2-brine (0.8 M NaCl)-quartz CA at a wide
346 range of pressures (0–400 bar) and 36 °C was found according to Farokhpoor et al.'s work [9],
347 where the substrate and brine salinity had noticeable influences on the CA. The discrepancies
348 observed in the literature may stem from differences in sample lithologies and mineral
349 occurrences, cleaning procedures, equilibration states, and measurement conditions and methods.

350 In addition, the contact angle method measures the wettability of a small piece of reservoir rock
351 which is not necessarily representative of the compositional and structural heterogeneity of
352 reservoir formations. This challenge of scale makes it difficult to use a small piece of rock to
353 represent the reservoir scale. However, these rock samples at the studied reservoir conditions all
354 showed water-wet behavior and became more water-wet as pressure increased, indicating that as
355 CO_2 injection continues, the rock could become more water-wet, making residual trapping more
356 effective. Instead of identifying the wettability of the formation with rock pieces, this last finding
357 is more important for the further understanding of the CO_2 storage process and the current
358 storage site.

359 **3.1.3. Capillary pressure interpretation for sealing formation Fuson and Opeche**

360 Laboratory capillary pressure data can be converted into reservoir conditions assuming the
361 studied samples are representative of the selected cap rock of interest:

362 $$Pc_{res} = Pc_{lab} \frac{[\sigma \cdot cos\theta]_{res}}{[\sigma \cdot cos\theta]_{lab}} \quad \text{(Eq. 3)}$$

363 where

364 Pc_{res} is the capillary pressure converted to reservoir conditions for the CO_2-SFW system,

365 Pc_{lab} is the capillary pressure measured under laboratory conditions for the mercury-air
366 system,

367 $[\sigma \cdot cos\theta]_{res}$ is the fluid system properties at the reservoir conditions for the CO_2-
368 SFW/CO_2-SFW-rock system,

369 $[\sigma \cdot cos\theta]_{lab}$ is the fluid system properties at the laboratory conditions for the mercury-
370 air/mercury-air-quartz system, where the $\sigma_{lab} = 485\ mN/m$ and $\theta = 136°$ were used for
371 the calculation [32,33].

372 The maximum height above the free water level at which CO_2 can be trapped by the cap rock is
373 [34]:

374 $$z_{max} = \frac{Pc_{res}}{(\rho_w - \rho_{CO_2}) \times 0.433} \quad \text{(Eq. 4)}$$

375 where 0.433 is a derived constant of suitable dimensions to allow an expression of the capillary
376 pressure in pounds per square inch, density in grams per cubic centimeter, and height in feet.
377 z_{max} includes the height of the continuous phase of CO_2 and the height of the transition zone.
378 The density was extrapolated from **Table 4**. The Pc_{res} and z_{max} results are listed in **Table 8**. As
379 stated earlier, the Opeche and Fuson are unreactive Siliceous shales, which makes capillary
380 pressure a suitable indicator of sealing capacity. Here, the Opeche formation shows extraordinary
381 sealing capacity, which suggests the underlying Minnelusa formations should be favored as the
382 main CO_2 storage reservoir.

383 **Table 8** Pc_{res} and z_{max} results for sealing formations Fuson and Opeche

Sample ID	θ_{lab} (°)	σ_{lab} (mN/m)	Pc_{lab} (psi)	θ_{res} (°)	σ_{res} (mN/m)	Pc_{res} (psi)	z_{max} (ft)
Fuson 7970	136	485	5500[1]	35.83	35.77	457.5	2123.9
Opeche 9329.3	136	485	8500[2]	34.60	35.40	710.6	4002.5

384 [1] Mercury injection capillary pressure measured for sample Fuson 7967; [2] Mercury injection capillary pressure measured for sample Opeche 9333.

3.2. CO_2 storage evaluation and macro-scale wettability determination

3.2.1. CO_2 storage potential

Both drainage and imbibition processes were conducted for the Lakota, Hulett, and Minnelusa core plugs; however, Lakota 8031.4, Hulett 8332.6, and Minnelusa C 9457.8 and 9464.2 imbibition processes were not performed successfully due to technical malfunctions. Thus, only the results of successful tests are reported here. For Lakota 8031.4, injection flow rates 0.2, 0.3, 0.4, and 0.5 g/min were adopted to evaluate the most time-efficient flow rates for the following experiments. **Fig. 8** displays the CO_2 storage potential during the drainage and imbibition processes of Lakota cores.

For Lakota 8031.4, the injected CO_2 PV was 8.64, and the final CO_2 storage potential was 45.9%. As shown in **Fig. 8a and 8b**, the injected CO_2 PV for Lakota 8035.4 was larger than that of Lakota 8031.4 (10.56 PV compared to 8.64 PV), and the final CO_2 storage potential of Lakota 8035.4 (42.0%) was smaller than that of Lakota 8031.4 (45.9%). Additionally, the porosity of two Lakota core plugs is close, while the permeability of Lakota 8031.4 is larger (20.802 mD compared to 13.105 mD), representing better connectivity of the pore network in that part of the formation. However, the gas breakthrough pressure occurred at 0.36 PV and 0.25 PV for Lakota 8031.4 and 8035.4, respectively. Better pore connectivity but slower gas breakthrough makes it reasonable to speculate that the less water-wet characteristic of Lakota 8031.4 caused the larger CO_2 storage potential. Slowing down the gas breakthrough rate is the key to successful water displacement and maximizing the efficient storage of CO_2. The imbibition was conducted for Lakota 8035.4, where the SFW injection rate was 0.2 mL/min. The imbibition process (**Fig. 8c**) lasted for 8.70 SFW PV, and the residual CO_2 saturation was 5.9%. For the actual CO_2 storage project, since a large amount of SFW is not re-injected into the CO_2-occupied reservoir to

replace the CO_2, it is expected that the CO_2 saturation will be much larger than this pessimistic value.

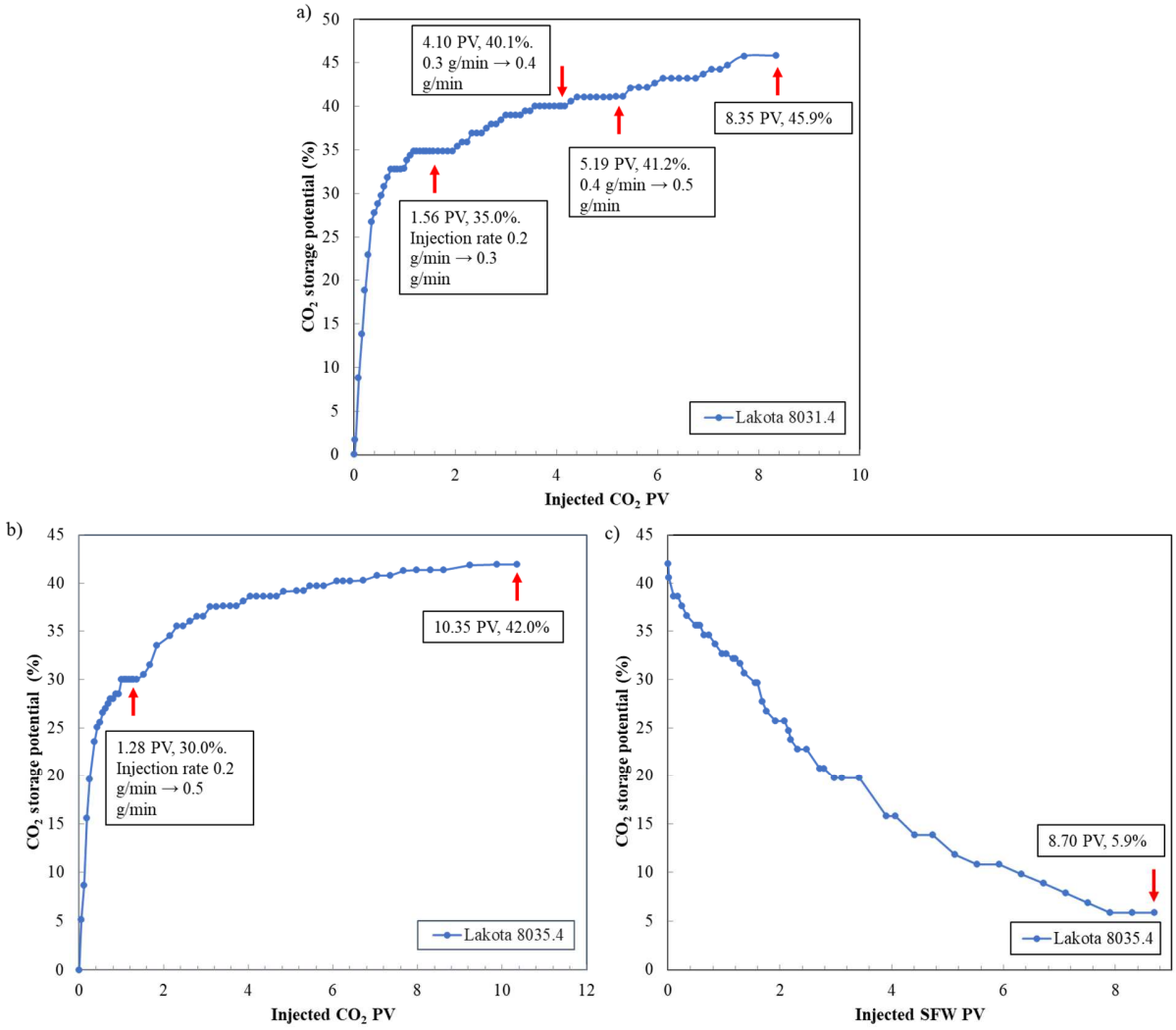

Fig. 8(a) Lakota 8031.4 sandstone drainage process at 2923 psi and 178 °F/81.1 °C; (b) Lakota 8035.4 sandstone drainage process at 2929 psi and 179 °F/81.7 °C; (c) Lakota 8035.4 sandstone imbibition process at 2929 psi and 179 °F/81.7 °C.

In **Table 2,** it is clear that the porosity of Lakota and Hulett core plugs is comparable, while the Hulett permeability is lower. Hulett 8307.7 has distinctive low porosity and ultra-low permeability, reflecting the intermittent ultra-tight and tight layers caused by calcite cementation in the Hulett formation. The CO_2 storage potential evaluations (**Fig. 9**) were carried out for Hulett 8307.7, Hulett 8325.8, and Hulett 8332.6. **Fig. 9a, 9b, and 9c** show that the CO_2 storage

potentials of Hulett 8307.7, Hulett 8332.6, and Hulett 8325.8 are 53.0%, 47.3% and 42.0%, respectively. For the imbibition test, due to a substantial pressure drop across the core plug when injecting SFW at 0.2 mL/min, the injection rate was reduced to 0.05 mL/min for Hulett 8307.7. Even though the imbibition process was not performed to completion, as can be seen in the pressure drop across the core plug at the end of the imbibition process, the results are worth mentioning. For Hulett 8307.7, there was a 0.318 CO_2 saturation decrease during the imbibition process after 2.26 PV SFW injection, but still, a large amount of CO_2 was trapped in this ultra-tight core plug. On the other hand, 10.2% of water was trapped in Hulett 8325.8.

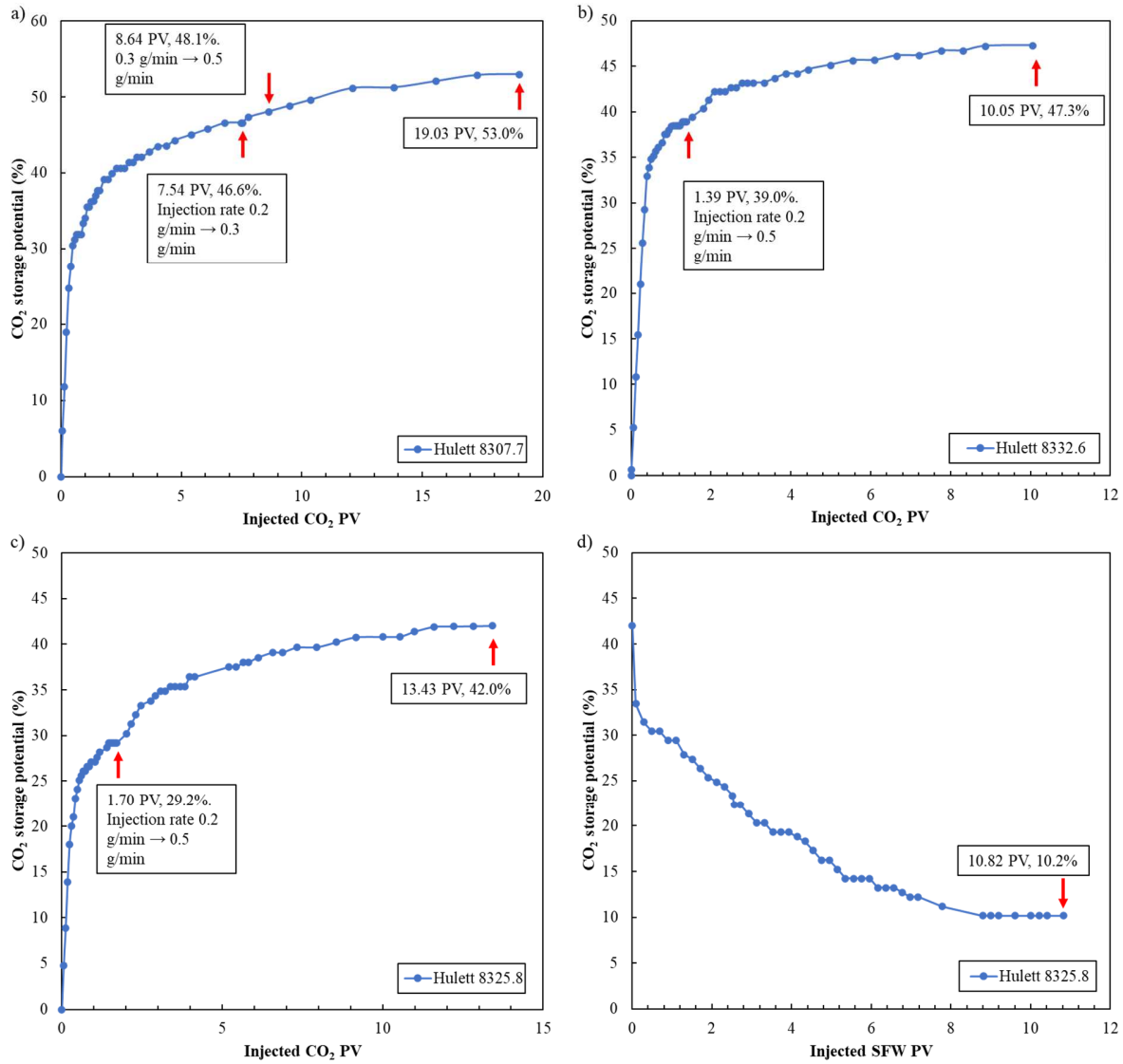

Fig. 9 (a) Hulett 8307.7 sandstone drainage process at 3303 psi and 182 °F/83.3 °C; (b) Hulett 8332.6 sandstone drainage process at 3337 psi and 183 °F/83.9 °C; (c) Hulett 8325.8 sandstone drainage process at 3328 psi and 183 °F/83.8 °C; (d) Hulett 8325.8 sandstone imbibition process at 3328 psi and 183 °F/83.8 °C.

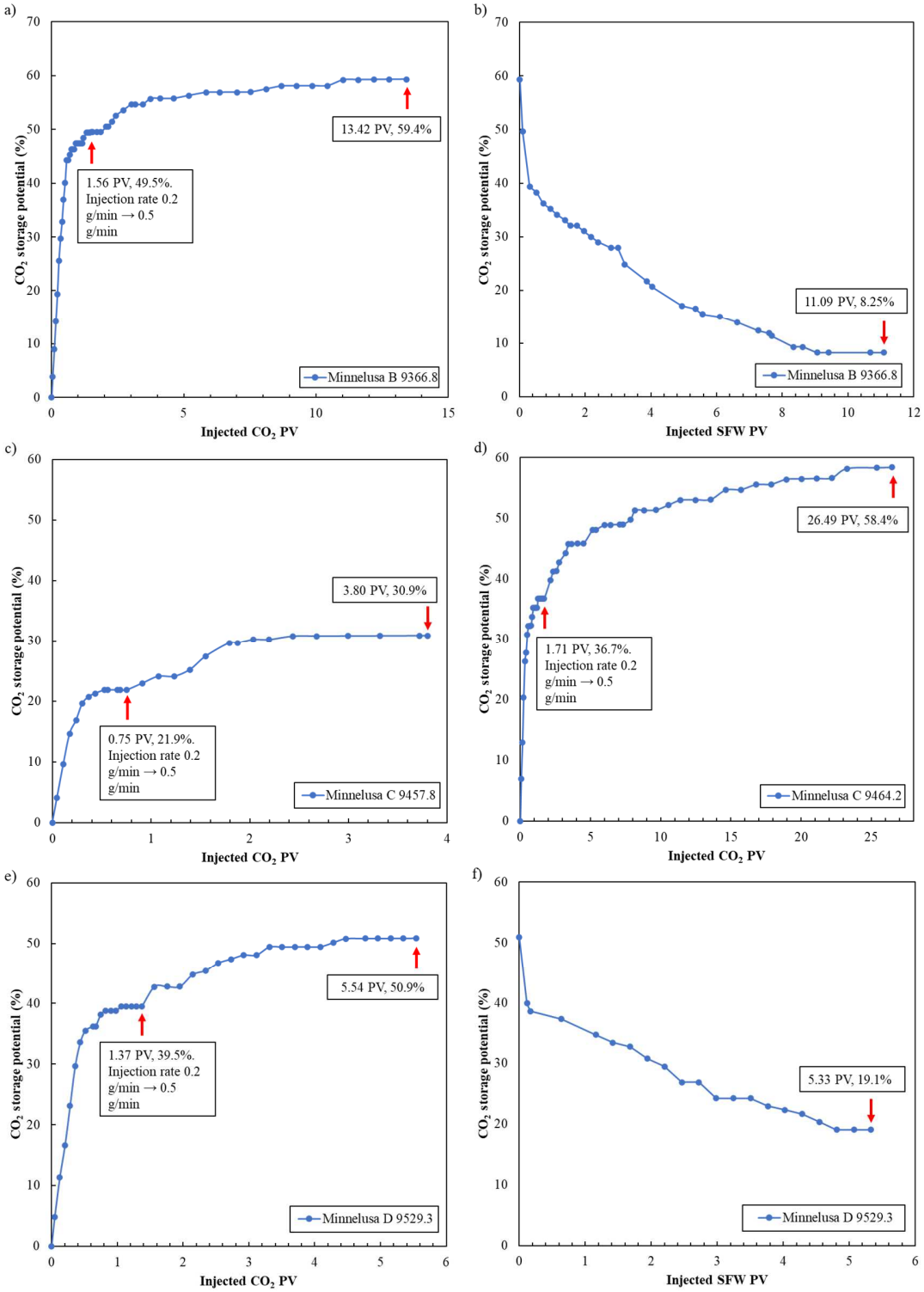

Fig. 10(a) Minnelusa B 9366.8 sandstone drainage process at 3814 psi and 181 °F/82.8 °C; (b) Minnelusa B 9366.8 sandstone imbibition process at 3814 psi and 181 °F/82.8 °C; (c) Minnelusa C 9457.8 sandstone drainage process at 3939 psi and 193 °F/89.2 °C; (d) Minnelusa C 9464.2 sandstone drainage process at 3945 psi and 193 °F/89.4 °C; (e) Minnelusa D 9529.3 sandstone drainage process at 4007 psi and 202 °F/94.2 °C; (f) Minnelusa D 9529.3 sandstone imbibition process at 4007 psi and 202 °F/94.2 °C.

Fig. 10 illustrates the drainage and imbibition results of Minnelusa core plugs. It is important to mention that the Minnelusa B formation has the highest CO_2 storage potential of all tested core samples in this study (**Fig. 10a and 10b**). Meanwhile, Minnelusa C 9457.8 represent Minnelusa C as a heterogeneous formation, where CO_2 would bypass this high permeability region. However, it shows the heterogeneity of the Minnelusa formation due to aeolian deposition. This sample was selected to demonstrate the injectivity effect on CO_2 storage in such a system. **Fig. 10c** shows that at a fixed injection rate schedule, CO_2 mobilizes very well in this well-connected sample and is prone to bypass much of the core plug through channelized flow. This results in a 30.9% CO_2 storage potential. On the other hand, Minnelusa C 9464.2 was selected rigorously, representing the Minnelusa C formation primarily in the porosity and permeability. **Fig. 10d** displays the drainage process of Minnelusa C 9464.2. The Minnelusa C 9464.2 shows higher CO_2 storage potential than both Lakota and Hulett samples. Meanwhile, the Minnelusa C sample exhibits similarities compared to the Minnelusa B sample. **Fig. 10e and 10f** illustrate the drainage and imbibition processes of Minnelusa D 9529.3, where Minnelusa D 9529.3 shows a slightly lower CO_2 storage potential compared to Minnelusa B and C.

3.2.2. Relative permeability and macro-scale wettability interpretation

Fig. 11 summarizes the drainage relative permeability interpretation of the Lakota, Hulett, and Minnelusa core samples adopting the modified Brooks and Corey (MBC) model [35].

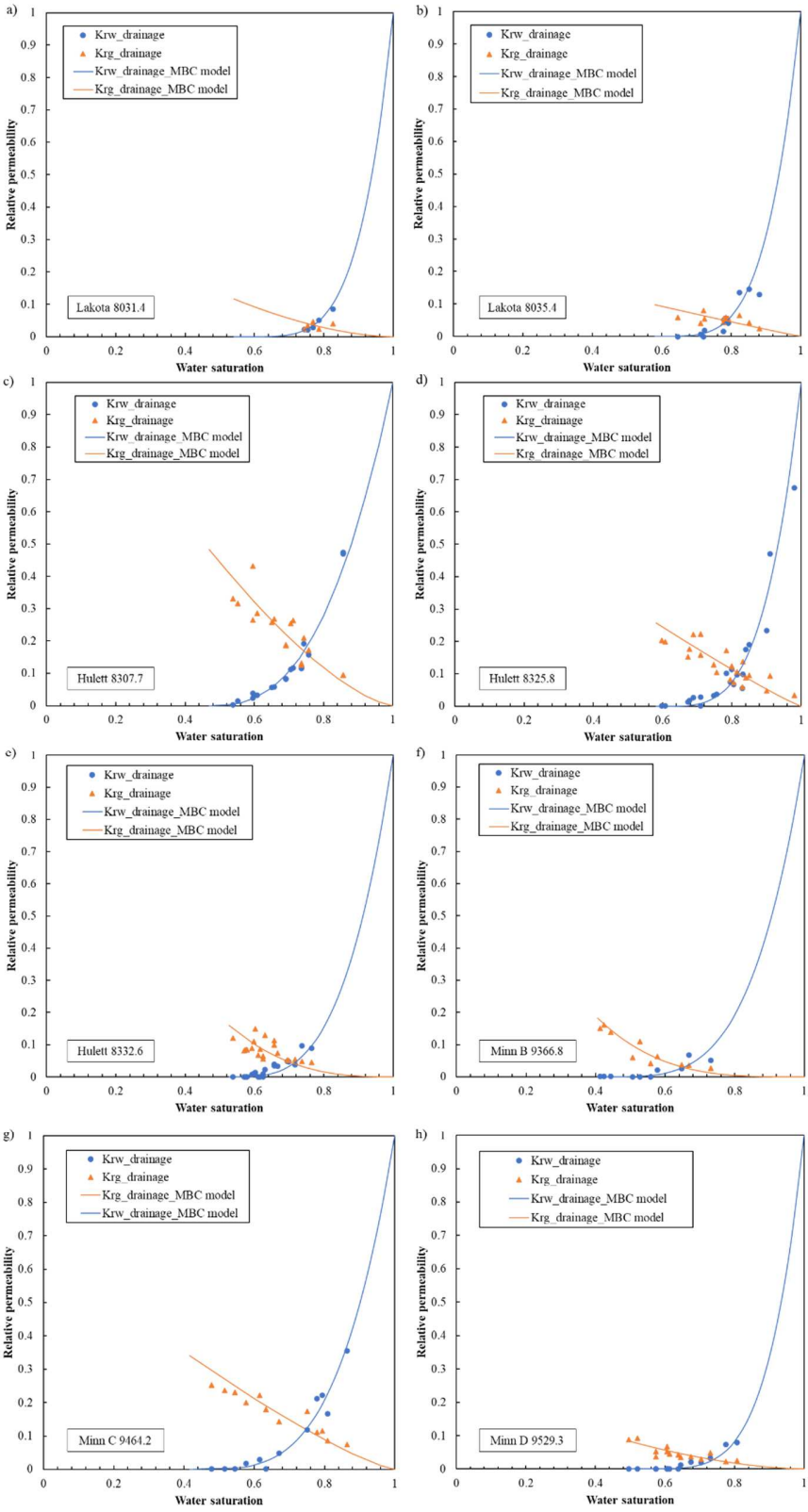

455

456 **Fig. 11** Drainage relative permeability interpretations of the Lakota, Hulett, and Minnelusa core samples.

457 The macro-scale wettability—wettability index of the samples is interpreted from the drainage
458 relative permeability using Craig's three rules of thumb [15,16], where the Lax Index I_{kr} is
459 introduced [16]. Craig assumed a 50% water saturation as the reference crossover saturation
460 (RCS) to compare the crossover point saturation derived from relative permeability curves, while
461 Mirzaei-Paiaman revisited Craig's rules of thumb and argued that the saturation change occurs
462 only in a portion of the connected space and it is case-specific. As a result, RCS was defined as
463 50% of the dynamic space. For a strongly water-wet sample I_{kr} advances toward $+1$, otherwise
464 I_{kr} tends to -1. For our approach, Craig's first rule was not applicable. Thus, the alternative I_{kr}
465 was adopted [16], which focuses on Craig's second and third rules. **Table 9** lists the I_{kr}
466 calculation.

467 **Table 9** Wettability Index

Sample No.	I_{kr}	I_{kr_ave}
Lakota 8031.4	0.702	0.717
Lakota 8035.4	0.731	
Hulett 8307.7	0.651	0.681
Hulett 8325.8	0.769	
Hulett 8332.6	0.624	
Minnelusa B 9366.8	0.505	0.594
Minnelusa C 9464.2	0.644	
Minnelusa D 9529.3	0.632	

468

469 The relative permeability interpretation suggests that the Lakota, Hulett, and Minnelusa samples
470 behave strongly to moderately water-wet behaviors, varying with the depths. Overall, Minnelusa
471 is less water-wet than Hulett and Lakota. **Fig. 12** displays the thin section images for the rock
472 samples at the selected depths. The microcrystalline dolomite cement presented in a significant
473 amount shown in Minnelusa B 9366.8 and Minnelusa C 9464.2 should be the reason that upper
474 Minnelusa showed less water-wet behavior.

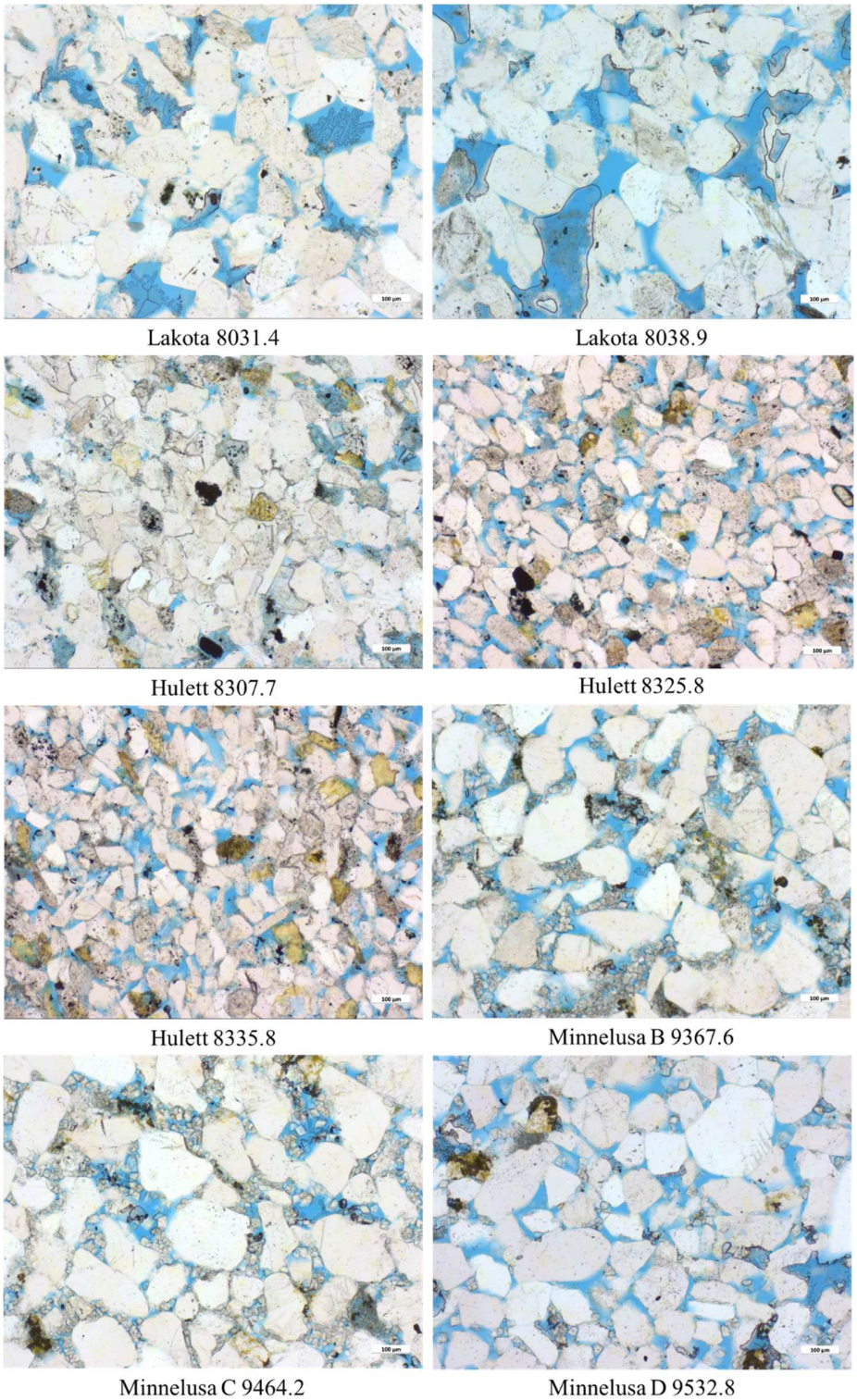

475

476 **Fig. 12** Thin section images. Note the images of Lakota 8038.9, Hulett 8335.8, and Minnelusa D 9532.8 are
477 substitutions for Lakota 8035.4, Hulett 8325.8 and 8332.6, and Minnelusa D 9529.3. The thin section description for
478 these three sets is mostly identical, especially for the dolomite cement description.
479

3.3. Connectivity, wettability, and their effect on CO_2 storage capacity

Table 10 and Fig. 13 display the CO_2 storage summary for tested reservoir core plugs. Overall, the highest CO_2 storage potential is found in Minnelusa core plugs, with an average of 56.2% than in Hulett (47.4%) and Lakota (43.9%) core plugs. When taking porosity into account, the average CO_2 storage capacities for Lakota, Hulett, and Minnelusa are about 6.0%, 5.7%, and 6.0%, respectively. When considering storage capacity, CO_2 injectate activity, and sealing potential, the upper Minnelusa region is the most favorable among Lakota, Hulett, and Minnelusa formations. This region of the upper Minnelusa is further enhanced by the good sealing capacity of the Opeche cap rock (**Section 3.1.3**). If CO_2 were to be emplaced and later displaced by water, all formations would have similar CO_2 trapping performance (average at ~1.3%). In general, selecting the target storage formation is a systematic process, where CO_2 storage capacity during injection and whether water is re-injected or not should all be considered. The decision should be made based on the approach and goal of the project.

Table 10 CO_2 storage summary for the representative reservoir core plugs

Sample No.	Permeability (mD)	Porosity	CO_2 storage potential	CO_2 storage potential – after imbibition	CO_2 storage capacity	CO_2 storage capacity – after imbibition
Lakota 8031.4	20.8	13.5%	45.9%	-	6.2%	-
Lakota 8035.4	13.1	13.9%	42.0%	5.9%	5.8%	0.8%
Hulett 8307.7	0.006	9.1%	53.0%	-	4.8%	-
Hulett 8325.8	2.2	13.1%	42.0%	10.2%	5.5%	1.3%
Hulett 8332.6	5.3	14.3%	47.3%	-	6.8%	-
Minnelusa B 9366.8	8.7	12.8%	59.4%	8.3%	7.6%	1.1%
Minnelusa C 9464.2	2.0	9.0%	58.4%	-	5.3%	-
Minnelusa D 9529.3	18.8	10.1%	50.9%	19.1%	5.1%	1.9%

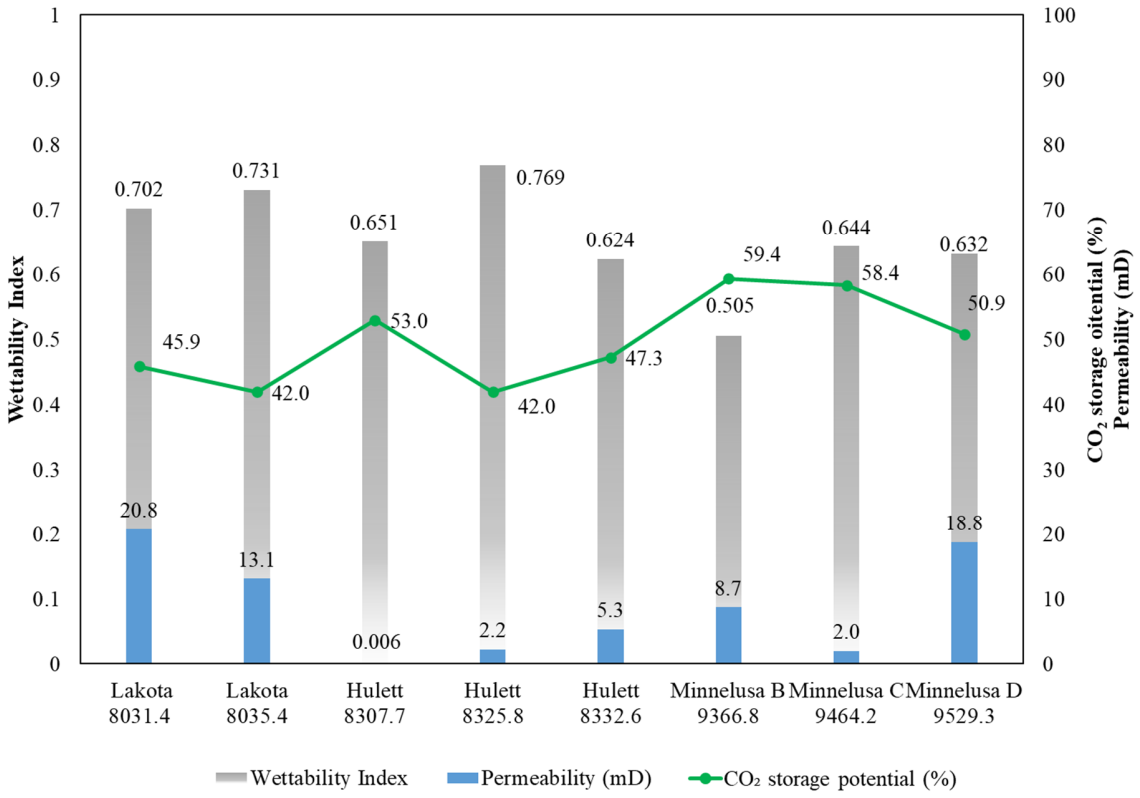

Fig. 13 Summary of the wettability, permeability, and CO_2 storage potential for all tested core samples.

If injectivity could be guaranteed regardless of low permeability, then the lower permeabilities and less water-wet formations promote higher CO_2 storage potential during the drainage process. Yet, the weight of these two factors when identifying the ideal balance remains less discussed. As mentioned earlier, for Lakota 8031.4, higher permeability (permeability difference of 7.7 mD) but slower gas breakthrough makes it reasonable to predict that the less water-wet characteristic of Lakota 8031.4 resulted in the larger CO_2 storage potential than Lakota 8035.4. Thus, here, permeability weighs less than wettability, similar to Hulett 8325.8 and 8332.6. On the other hand, Hulett 8307.7 has ultra-low permeability that favours the highest CO_2 storage potential among Hulett samples. Nevertheless, regression analysis was performed for I_{kr}, permeability, and CO_2 storage potential. Permeability appears to be much less of a factor in the CO_2 storage potential

than the wettability (**Fig. 14**), where the latter impacts the CO_2 storage potential performance more significantly during the drainage process, which sets the baseline for the long-term CO_2 residual trapping.

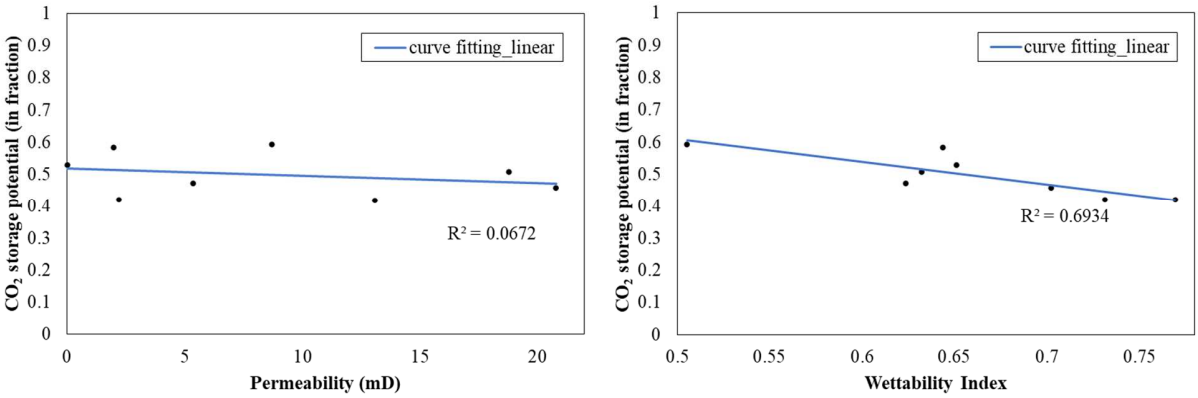

Fig. 14 The tentative correlation between I_{kr}, permeability, and CO_2 storage potential for the drainage process

As previously defined, the CO_2 storage potential in this work focuses on the pore space utilization aspect, and the discussion about the correlation between connectivity, wettability, and CO_2 storage potential was logical. Yet, when the CO_2 storage potential term is expanded (CO_2 storage potential*) to consider the solubility trapping, the solubility term could be added assuming fully CO_2-saturated residual formation water:

$$CO_2\ storage\ potential^*\ (\%) = CO_2\ storage\ potential + (1 - CO_2\ storage\ potential) \times CO_2\ solubility \quad \text{(Eq. 5)}$$

The CO_2 solubility in the respective formation water and the expanded CO_2 storage potential* values are listed in **Table 11**. The expanded CO_2 storage potential* follows the same trend as the CO_2 storage potential, as the displaced formation water provides more capacity for CO_2 storage.

Table 11 CO_2 solubility and expanded CO_2 storage potential*

Sample No.	CO_2 solubility (mL/mL) [28,29]	CO_2 storage potential*
Lakota 8031.4	0.0611	49.2%
Lakota 8035.4	0.0609	45.5%
Hulett 8307.7	0.0425	55.0%
Hulett 8325.8	0.0423	44.5%
Hulett 8332.6	0.0422	49.5%
Minnelusa B 9366.8	0.0386	61.0%
Minnelusa C 9464.2	0.0528	60.6%
Minnelusa D 9529.3	0.0389	52.8%

Considering the imbibition, the degree of residual trapping is dictated by wettability, pore-throat size ratio, and pore connectivity [5]. Specifically, maximizing residual trapping requires the selection of highly water-wet, large pore-throat size ratio, and poor connectivity rocks. The pore-throat size ratio was not evaluated for the selected samples. Thus, the discussion is based on wettability and connectivity. Nevertheless, the pore-throat ratio analysis will be addressed in future work. As shown in **Table 10**, the lower permeability (494% difference, poorer connectivity) and nearly equal I_{kr} (5% difference, similar wettability) Hulett 8325.8 sample trapped 74% more CO_2 (storage potential) compared to the Lakota 8035.4 sample, which is in agreement with Krevor et al. [5]. For Minnelusa B 9366.8 and Minnelusa D 9529.3, the higher permeability (115% difference, better connectivity) and higher I_{kr} (25% difference, more water-wet) Minnelusa D 9529.3 trapped far more CO_2 (131% difference) than the Minnelusa B 9366.8 sample. Here, the wettability shadowed the reverse effect of connectivity. Although more data is required to make a solid conclusion, these limited data may suggest that wettability is a dominant factor for residual trapping. Recall the discussion from **Section 3.1.2**: for the rock samples and respective reservoir conditions adopted in this study, the CA decreases (more water-wet) when

pressure increases during CO_2 injection. Then, this wettability change discourages further CO_2 storage potential, yet benefits the CO_2 residual trapping as the CO_2 injection proceeds.

4. Conclusion

This study selected representative samples from the target storage formations (the Lower Cretaceous Lakota Sandstone, Jurassic Hulett Sandstone, and Pennsylvanian Minnelusa Formation near DFS) for the micro-scale wettability (CA measurement), macro-scale wettability (wettability index derived from unsteady-state flow characterization for the core plugs), and CO_2 storage capacity evaluation. The conclusions are summarized as follows:

- The micro- and macro-wettability characterizations suggest that the Lakota, Hulett, and Minnelusa samples behave strongly to moderately water-wet. Overall, Minnelusa is less water-wet than Hulett and Lakota.
- The highest CO_2 storage potential is found in Minnelusa core plugs, with an average of 56.2% compared with the Hulett (47.4%) and Lakota (43.9%) samples. The average CO_2 storage capacities for Lakota, Hulett, and Minnelusa are about 6.0%, 5.7%, and 6.0%, respectively. Meanwhile, the lower Hulett formation and Minnelusa B sandstone region have slightly better CO_2 storage capacity due to their distinctive lithologies.
- The Opeche Shale formation shows extraordinary sealing capacity, which suggests the underlying Minnelusa formations should be favored as the main CO_2 storage reservoir.
- Wettability appears to dominate the CO_2 storage potential performance during drainage, where less water-wet behavior promotes higher CO_2 storage potential. As for residual trapping, it is most significant in highly water-wet, large pore-throat size ratio, and poor connectivity rocks. Although more data is required to make a solid conclusion, the limited data shown in this work may suggest that wettability is a dominant factor for residual

565 trapping. For the rock and water samples and respective reservoir conditions adopted in this
566 study, the CA decreases (more water-wet) when pressure increases during CO_2 injection.
567 Then, this wettability change discourages further CO_2 storage potential yet benefits the CO_2
568 residual trapping as the CO_2 injection proceeds.

569 • Even though representative rocks were assessed with lots of effort, the reservoir is
570 heterogeneous as its nature; this much of the labor is still inadequate for a more robust
571 reservoir profile. Therefore, more samples representing the heterogeneity should also be
572 evaluated, as well as the samples taken from the nearby wells. Meanwhile, further pore-throat
573 ratio analysis will be addressed for our better understanding of residual trapping.

574 Overall, the work presented in this study provides valuable insights into wettability's effect on
575 the CO_2 storage capacity and wettability's importance when identifying the optimal CO_2 storage
576 formation to meet the project's goals.

577 **Acknowledgements**

578 The authors would like to thank the Department of Energy for funding through the grant DE-
579 FE0031891. We also thank Dr. John Oakey (University of Wyoming) for allowing us to use the
580 Olympus LEXT OLS4000 3D Laser Scanning Microscope.

581 **Reference**

582 [1] Cuéllar-Franca RM, Azapagic A. Carbon capture, storage and utilisation technologies: A
583 critical analysis and comparison of their life cycle environmental impacts. J CO2 Util
584 2015;9:82–102. https://doi.org/10.1016/j.jcou.2014.12.001.

585 [2] Fankhauser S, Smith SM, Allen M, Axelsson K, Hale T, Hepburn C, et al. The meaning of
586 net zero and how to get it right. Nat Clim Chang 2022;12:15–21.
587 https://doi.org/10.1038/s41558-021-01245-w.

588 [3] Fajardy M, Mac Dowell N. Can BECCS deliver sustainable and resource efficient
589 negative emissions? Energy Environ Sci 2017;10:1389–426.
590 https://doi.org/10.1039/c7ee00465f.

[4] Metz B, Davidson O, Coninck H de, Loos M, Meyer L (Eds. . IPCC Special Report on Carbon Dioxide Capture and Storage. 2005.

[5] Krevor S, Blunt MJ, Benson SM, Pentland CH, Reynolds C, Al-Menhali A, et al. Capillary trapping for geologic carbon dioxide storage - From pore scale physics to field scale implications. Int J Greenh Gas Control 2015;40:221–37. https://doi.org/10.1016/j.ijggc.2015.04.006.

[6] Yu Y, Hanamertani AS, Korsah PK, Jiao Z, McLaughlin JF. Feasibility of Bulk CO2-Foam Screening for Carbon Storage Evaluations at Reservoir Conditions. SPE West Reg Meet Proc 2022;2022-April. https://doi.org/10.2118/209315-MS.

[7] Sarmadivaleh M, Al-Yaseri AZ, Iglauer S. Influence of temperature and pressure on quartz-water-CO2 contact angle and CO2-water interfacial tension. J Colloid Interface Sci 2015;441:59–64. https://doi.org/10.1016/j.jcis.2014.11.010.

[8] Saraji S, Goual L, Piri M, Plancher H. Wettability of supercritical carbon dioxide/water/quartz systems: Simultaneous measurement of contact angle and interfacial tension at reservoir conditions. Langmuir 2013;29:6856–66. https://doi.org/10.1021/la3050863.

[9] Farokhpoor R, Bjørkvik BJA, Lindeberg E, Torsæter O. Wettability behaviour of CO2 at storage conditions. Int J Greenh Gas Control 2013;12:18–25. https://doi.org/10.1016/j.ijggc.2012.11.003.

[10] McPhee C, Reed J, Zubizarreta I. Wettability and Wettability Tests. vol. 64. 2015. https://doi.org/10.1016/B978-0-444-63533-4.00007-X.

[11] Donaldson EC, Thomas RD, Lorenz PB. Wettability Determination and Its Effect on Recovery Efficiency. Soc Pet Eng J 1969;9:13–20. https://doi.org/10.2118/2338-PA.

[12] Farzana S, Baldygin A, Waghmare PR. Experimental and theoretical investigation of the effects of pressure on the hydrodynamically driven droplet spreading. Chem Eng Sci 2022;254:117644. https://doi.org/10.1016/j.ces.2022.117644.

[13] Farzana S, Baily R, Waghmare PR. Study of early time dynamics of drop spreading in different surrounding pressure. Exp Therm Fluid Sci 2021;128:110450. https://doi.org/10.1016/j.expthermflusci.2021.110450.

[14] Amott E. Observations Relating to the Wettability of Porous Rock. Trans AIME 1959;216:156–62. https://doi.org/10.2118/1167-g.

[15] Anderson WG. Wettability Literature Survey - Part 5: the Effects of Wettability on Relative Permeability. JPT, J Pet Technol 1987;39:1453–68. https://doi.org/10.2118/16323-PA.

[16] Mirzaei-Paiaman A. New methods for qualitative and quantitative determination of wettability from relative permeability curves: Revisiting Craig's rules of thumb and introducing Lak wettability index. Fuel 2021;288:119623. https://doi.org/10.1016/j.fuel.2020.119623.

[17] Gant PL, Anderson WG. Core Cleaning for Restoration of Native Wettability. SPE Form

Eval 1988;3:131–8. https://doi.org/10.2118/14875-PA.

[18] Fertl WH, Chilingarian G V., Rieke HHI, editors. Abnormal formation pressure environments. Dev. Pet. Sci., vol. 2, Elsevier; 1976, p. 1–48. https://doi.org/10.1016/S0376-7361(08)70023-2.

[19] Spencer CW. Hydrocarbon generation as a mechanism for overpressuring in Rocky Mountain region. Am Assoc Pet Geol Bull 1987;71:368–88. https://doi.org/10.1306/94886eb6-1704-11d7-8645000102c1865d.

[20] Zhang JJ. In situ stress estimate. 2019. https://doi.org/10.1016/b978-0-12-814814-3.00006-x.

[21] Zhu W, Wong T. The transition from brittle faulting to cataclastic flow: Permeability evolution. J Geophys Res Solid Earth 1997;102:3027–41. https://doi.org/10.1029/96jb03282.

[22] Braun EM, Blackwell RJ. A steady-state technique for measuring oil-water relative permeability curves at reservoir conditions. Proc - SPE Annu Tech Conf Exhib 1981;1981-Octob. https://doi.org/10.2118/10155-ms.

[23] Johnson EF, Bossler DP, Bossler VON. Calculation of Relative Permeability from Displacement Experiments. Trans AIME 1959;216:370–2. https://doi.org/10.2118/1023-g.

[24] Bennion DB, Bachu S. Drainage and imbibition relative permeability relationships for supercritical CO2/brine and H2S/brine systems in intergranular sandstone, carbonate, shale, and anhydrite rocks. SPE Reserv Eval Eng 2008;11:487–96. https://doi.org/10.2118/99326-pa.

[25] Richardson JG, Kerver JK, Hafford JA, Osoba JS. Laboratory Determination of Relative Permeability. J Pet Technol 1952;4:187–96. https://doi.org/10.2118/952187-G.

[26] NIST Chemistry WebBook. 2021. https://doi.org/https://doi.org/10.18434/T4D303.

[27] Ouyang LB. New correlations for predicting the density and viscosity of supercritical carbon dioxide under conditions expected in carbon capture and sequestration operations. Open Pet Eng J 2011;4:13–21. https://doi.org/10.2174/1874834101104010013.

[28] Duan Z, Sun R, Zhu C, Chou IM. An improved model for the calculation of CO2 solubility in aqueous solutions containing Na+, K+, Ca2+, Mg2+, Cl-, and SO42-. Mar Chem 2006;98:131–9. https://doi.org/10.1016/j.marchem.2005.09.001.

[29] Duan Z, Sun R. An improved model calculating CO2 solubility in pure water and aqueous NaCl solutions from 273 to 533 K and from 0 to 2000 bar. Chem Geol 2003;193:257–71. https://doi.org/10.1016/S0009-2541(02)00263-2.

[30] Chiquet P, Broseta D, Thibeau S. Wettability alteration of caprock minerals by carbon dioxide. Geofluids 2007;7:112–22. https://doi.org/10.1111/j.1468-8123.2007.00168.x.

[31] Fanchi JR. Rock–Fluid Interaction. Princ. Appl. Reserv. Simul., Elsevier; 2018, p. 81–99. https://doi.org/10.1016/B978-0-12-815563-9.00005-7.

[32] Ethington EF. Interfacial contact angle measurements of water, mercury, and 20 organic

668 liquids on quartz, calcite, biotite, and Ca-montmorillonite substrates. United States Geol
669 Surv 1990;90–409:1–18.

670 [33] Pirard R, Pirard JP. Mercury porosimetry applied to precipitated silica. Stud Surf Sci Catal
671 2000;128:603–11. https://doi.org/10.1016/s0167-2991(00)80066-x.

672 [34] Derrell A. Smith (2). Theoretical Considerations of Sealing and Non-Sealing Faults. Am
673 Assoc Pet Geol Bull 1966;50:363–74. https://doi.org/10.1306/5D25B48F-16C1-11D7-
674 8645000102C1865D.

675 [35] Behrenbruch P, Goda HM. Two-phase relative permeability prediction: A comparison of
676 the modified Brooks-Corey Methodology with a new carman-kozeny based flow
677 formulation. Proc - SPE Asia Pacific Oil Gas Conf Exhib 2006 Thriving Volatility
678 2006;2:810–27. https://doi.org/10.2118/101150-ms.

679

680